frontiers | Frontiers in Earth Science

TYPE Original Research
PUBLISHED 01 September 2023
DOI 10.3389/feart.2023.1223785

OPEN ACCESS

EDITED BY
Jia-wen Zhou,
Sichuan University, China

REVIEWED BY
Chong Xu,
Ministry of Emergency Management, China
Huazhe Jiao,
Henan Polytechnic University, China
Erol Yilmaz,
Recep Tayyip Erdoğan University, Türkiye
Xiaocheng Huang,
Hunan University of Science and Technology, China

*CORRESPONDENCE
Wei Sun,
kmustsw@kust.edu.cn

RECEIVED 16 May 2023
ACCEPTED 14 August 2023
PUBLISHED 01 September 2023

CITATION
Li Z-r, Jiang M-g, Feng X-l, Wang S-y, Zeng Q-t, Chen C, Liu W-l and Sun W (2023), Analysis of energy consumption characteristics and fracture characteristics of moraine grouting solidified body under uniaxial compression.
Front. Earth Sci. 11:1223785.
doi: 10.3389/feart.2023.1223785

Analysis of energy consumption characteristics and fracture characteristics of moraine grouting solidified body under uniaxial compression

Zheng-rong Li[1,2], Ming-gui Jiang[1], Xing-long Feng[2], Shao-yong Wang[3], Qing-tian Zeng[2], Chong Chen[3], Wen-lian Liu[4] and Wei Sun[1]*

[1]Faculty of Land and Resources Engineering, Kunming University of Science and Technology, Kunming, China, [2]Yunnan Diqing Non-Ferrous Metal Co, Ltd, Diqing, China, [3]School of Civil and Resources Engineering, University of Science and Technology Beijing, Beijing, China, [4]China Non-ferrous Metal Industry Kunming Exploration Design Research Institute, Kunming, China

Glacial movement causes massive accumulation of fine-grained moraine, which often induces slope instability, moraine debris flow, and other geological hazards due to the effects of rain and the ice-snow melting. This study used a modified phosphoric acid-water glass slurry for grouting and curing moraine, and analyzed the influencing law of water glass Baume degree and curing age on energy consumption characteristics as well as the fracture properties of the grout-cured body of moraine using the uniaxial compression test. The results showed that the gel time of phosphoric acid-water glass slurry increased with the increasing addition of phosphoric acid and that it had a mutation phenomenon. The gel time increased linearly with the increasing addition of phosphoric acid before the mutation. Moreover, the compressive strength, pre-peak total energy, pre-peak elastic energy, pre-peak dissipative energy, elastic energy density, dissipative energy density, and pre-peak fracture toughness of the moraine curing body at same curing age increased linearly with the increase of water glass Baume degree by 46%–218%. The compressive strength, pre-peak elastic energy, and pre-peak elastic energy density of the moraine curing body increased with the curing age but grew slowly from 3 days to 7 days and rapidly from 7 days to 14 days. Through regression analysis of the test results, the fracture toughness calculation formula was derived from an energy perspective. These research results have significant implications for the reinforcement of moraine strata grouting and glacial debris flow disaster prevention and control.

KEYWORDS

moraine, phosphoric acid-water glass, grouting reinforcement, energy dissipation, fracture toughness

1 Introduction

The Pulang copper deposit has relatively complete Quaternary glacial relics, meaning that the overlying strata have many glacial deposits. These glacial deposits are comprised of sediment and stones that have been deposited during glacial movement, mainly composed of clay, silt, gravel, pebbles, and boulders. The grain size distribution is vast, the structure is

different, and there is no stratification (Hart, 1998; Evans et al., 2021). The transport force of glaciers gradually decreases as they melt, resulting in the accumulation of large amounts of fine-grained moraines, which provide a rich source of material for forming glacial debris flows (Meng et al., 2023). With the increase of mining depth and the expansion of the surface collapse area, once the flood season arrives, the rainfall in the mining area, upstream surface runoff, and snow melt water in high mountains drive the surface moraine cover layer (tens of meters and weathered, broken rock debris) into the collapse area, which can easily cause underground mudflow accidents (Zaginaev et al., 2019; Gao et al., 2022). To date, research by both domestic and foreign scholars on glacial debris flow has mostly focused on the formation mechanisms, evolutionary process, risk evaluation and monitoring, and early warning (Marr et al., 2002; Li et al., 2016; Medeu et al., 2022), but research on the specific prevention and control measures for moraine debris flow disasters is needed. In response to the above problems, grouting reinforcement is used to change the moraine from powder to block, improve the integrity and stability of the loose accumulation, and improve the mechanical properties of the moraine as well as to preserve the surface vegetation to the maximum extent (Zhang et al., 2021; Fan et al., 2023). It is therefore important to study the mechanical properties and bearing mechanism of the moraine slurry curing body for both the prevention and control of downhole mudflow and the evaluation of the slurry effect. Coulter et al. (Coulter and Martin, 2006) and others have performed jet grouting in the boring tunnel process of moraine and analyzed the surface settlement of the grouting by numerical simulation in reverse, and the results showed that the narrow settlement trough was formed because of the local shear zone caused by high pressure during jet grouting. Luo et al. (Luo et al., 2019) and others have investigated the effects of different temperatures and envelope pressures on the strength of moraine permafrost by triaxial compression tests, and the results showed that the strength envelope is nonlinear when the average stress is less than the consolidation yield pressure defined as the strength envelope boundary stress, while it is approximately linear when the average stress is greater than the consolidation yield pressure. Li et al. (Li et al., 2022) investigated the effect of different ice forms, such as crushed ice and block ice, on the mechanical properties of moraine soils by triaxial constant strain rate (CSR) with coupled thermomechanical (CTM) tests. The test results show that moraine soils containing block ice have higher peak strength and moraine soils containing crushed ice are more sensitive to temperature changes. Begam et al. (Begam et al., 2018) showed that the height of the moraine dam and the volume of the lake upstream of the dam are the most sensitive parameters affecting the GLOF peak using coupled numerical simulations and indoor similar experimental simulations to verify the moraine dam overflow and erosion damage. Peng et al. (Peng et al., 2022) derived the flow discharge, erosion, entrainment, and deposition processes of glacial debris flows through field investigations and numerical simulations, revealing the origin mechanism and dynamic evolution process of the debris-ice landslide-debris flow hazard chain. Because there are few studies on moraine grouting and curing at home and abroad, the study was conducted with reference to the test and evaluation methods of the strength of fractured rock after grouting. Weng et al. (Weng et al., 2022) showed that the infiltration grouting tests on fractured sandstone samples analyzed the flow and diffusion mechanism of the slurry, and the results showed that the final injection volume of grouting decreased with the increase of temperature and surrounding pressure, and the effective grouting time was inversely proportional to the slurry flow rate, while it was positively correlated with temperature. Zhang et al. (Zhang et al., 2022) investigated the mechanical properties of compressed pre-cracked sandstone before and after grouting by triaxial compression tests with different surrounding pressures, and the results showed that the strength of grouted specimens mainly depended on the micromechanical properties of the contact surface between sandstone and cement paste, and the elastic modulus of grouted specimens was lower than that of uncracked sandstone. Liu et al. (Liu et al., 2022) proposed an NMM-HM grouting model based on the numerical flow form method (NMM) to study the flow of slurry, and the results showed that the fracture grouting pressure could increase the fracture aperture, which is beneficial to grouting efficiency. Salimian et al. (Salimian et al., 2017) performed direct shear tests on grout cracks by preparing specimens with three different surface roughnesses using dental silica gel, and the test results showed that the compressive grout strength increased with decreasing water-cement ratio, but not necessarily with increasing shear strength. Sui et al. (Sui et al., 2015) showed that the two largest factors affecting the sealing efficiency were the initial water flow velocity and the width of the hole diameter, with the former having a greater effect than the latter. Kumar et al. (Kumar et al., 2022) studied the mechanical properties of intact specimens, ungrouted joints, cement joint grout, and epoxy joint grout specimens under dynamic and static loads, and the test results showed that the strength of the epoxy grout joint samples was all greater than that of the cement grout samples.

In summary, research on grouting reinforcement for moraine strata is still in the exploration and development stage. The overlying moraines of the Purang copper mine are mostly composed of fine clay wrapped with stones that are randomly distributed, and the permeability of the soil body is extremely poor under the double extrusion of glacial accumulation and geological movement. Figure 1A shows that the traditional cement slurry cannot be injected permeably. The cement particles and the moraine soil have a noticeable percolation effect. Many cement particles are retained on the moraine's surface to obstruct the continuous injection of the slurry. Because of the above engineering problems, the modified phosphoric acid-water glass slurry with better injectability is chosen to grout and cure the moraine, and its grouting effect is shown in Figure 1B; under the same grouting conditions, the slurry can be fully diffused in the moraine, and the slurry is distributed along both sides of the splitting channel and forms a large volume of slurry-soil complex at the end of the splitting track. After the grouting is completed, the grouting effect of the reinforced soil needs to be evaluated to determine the feasibility and sustainability of the grouting project. Therefore, this paper investigates the influence law of water glass Baume degree and curing age on moraine slurry curing body through a uniaxial compression test and discusses and analyzes the mechanical properties and energy consumption characteristics of moraine slurry curing, further revealing the damage mechanism of moraine slurry curing body and slurry consolidation mechanism. Based on the regression fitting analysis method, our study

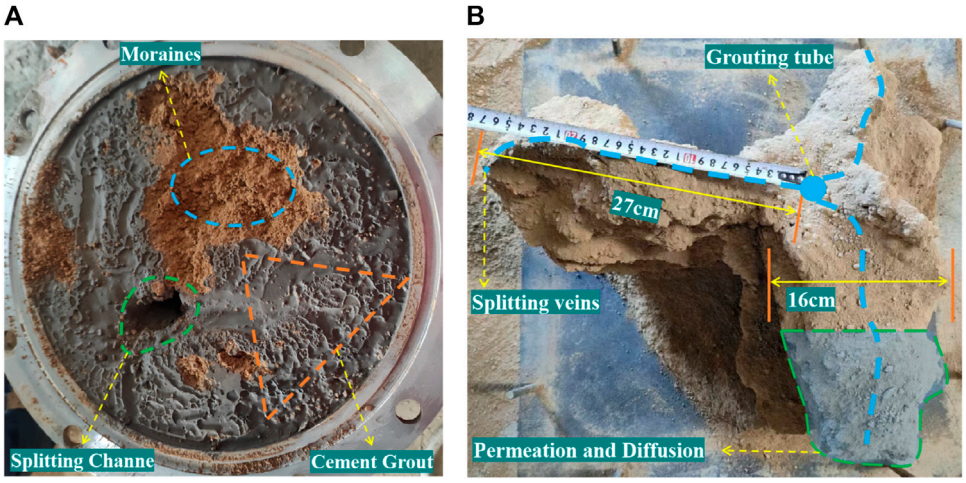

FIGURE 1
Dispersion distribution of different slurry injections: **(A)** cement slurry; **(B)** phosphoric acid-water glass slurry.

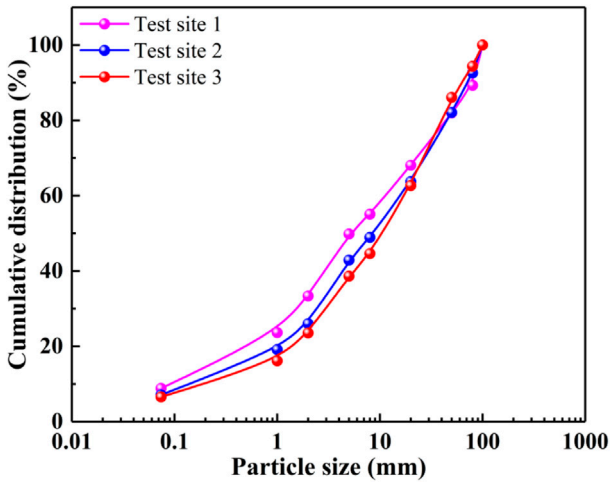

FIGURE 2
Moraine grain level composition curve.

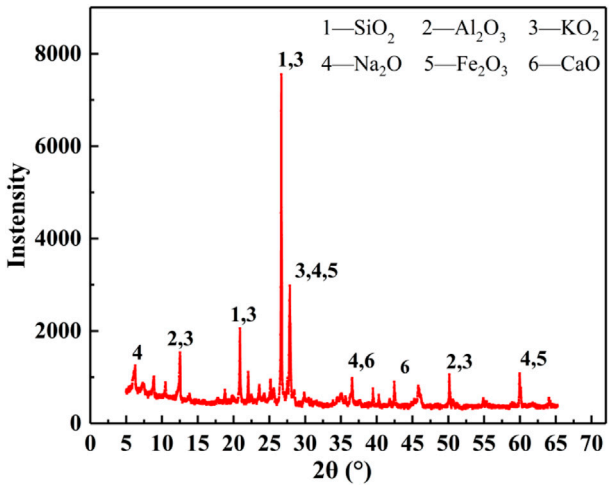

FIGURE 3
X-ray powder diffraction test spectra of moraines.

establishes a fracture toughness relationship model based on energy analysis and proposes an evaluation method for establishing slurry and the parameters and fracture toughness of the moraine slurry curing body. The results have great significance to engineering theories of moraine slurry reinforcement and the prevention and control of moraine debris flow disasters.

2 Experimental design

2.1 Test material

In this experiment, a modified phosphoric acid-water glass solution was chosen as the grouting material, and the water glass has a Baume degree of 35°B e' and a modulus of 3.05. The test water was ordinary tap water, and the moraine selected for the test was taken from the Pulang copper mine in Yunnan. According to the genesis of the formation, geotechnical type, and physical and mechanical properties, the soil within the 10 m exploration depth of the test site was divided into three layers, and the exploratory pit was excavated to take *in-situ* soil samples for each layer and carry out the test of physical and chemical indexes of the soil. According to the genesis of the stratum, geotechnical type, and physical and mechanical properties, the soil within the 10 m exploration depth of the test site was divided into three layers, pits were excavated, and *in-situ* soil samples were taken for each layer. The soil physicochemical index test was carried out, the grain-level composition and XRD patterns are shown in Figure 2 and Figure 3, respectively, and the chemical composition and basic properties of the original moraine formation are shown in Table 1 and Table 2, respectively. From

TABLE 1 X-ray powder diffraction analysis of moraines.

Quartz (%)	Albite (%)	Chlorite (%)	Mica (%)	Montmorillonite (%)	Illite (%)	Kaolinite (%)	Andesine (%)	Saspachite (%)	Pargasite (%)
28.8	24.8	14.9	16.1	0	0	0	6.9	3.3	5.2

TABLE 2 Basic properties of *in situ* stratigraphy.

Wet density/(kg/cm^3)	dry density (kg/cm^3)	Porosity/%	Permeability coefficient/(cm/s)	Plasticity limit/%	Liquid limit/%
2.29×10^3	2.21×10^3	17.21	8.95×10^{-5}	16	22

Figure 2, the moraine inhomogeneity coefficient is 113.43, and the curvature coefficient is 2.77, which indicates that the moraine is well-graded and dense. As can be seen from Table 1 and Figure 3, the main constituents of moraines are SiO_2, Na_2O-Al_2O_3-$6SiO_2$, and $KAl_2(AlSi_3O)$ $(OH)_2$, *etc.*, of which quartz and nannofeldspar account for about 53.6% of the total weight, feldspar and quartz are all stable minerals in nature and are widely found in nature, chlorite does not show special properties when exposed to water. It does not contain montmorillonite, illite, Kaolinite, and other water-sensitive minerals (Zhao et al., 2018; Yi et al., 2022). As can be seen from Table 2, the wet density of the moraine stratum is 2.29 g/cm^3, the dry density is 2.21 g/cm^3, the plastic limit of the soil is 16%, the liquid limit is 22% its low liquid limit powdery clay, the permeability coefficient of the soil is 8.95×10^{-5} cm/s for the weak permeability level.

2.2 Formulation of phosphoric acid-water glass slurry

The slurry gelation time in actual engineering grouting should be controlled from 30 to 60 min to ensure slurry penetration or diffusion in the grouted reinforced area (Cui et al., 2022). If the gel time is less than 30min, the slurry condenses prematurely, which blocks the grouting line, and if it is more than 60min, the slurry spreads too far in the formation and causes slurry loss. In this experiment, modified phosphoric acid-water glass chemical slurry was used as grouting material, and the suitable gel time of phosphoric acid-water glass slurry with different Baume degrees was explored. This test uses a water glass Baume degree of 35 and modulus of 3.05; phosphoric acid is selected as a medical phosphoric acid solution, with a concentration of 95%. The project examined two-liquid groutings and used diluted phosphoric acid and water glass solution with a volume ratio of 1:1 to carry out the test. First of all, according to the experimental design of water glass, the phosphoric acid solution is diluted with water to get the concentration of water glass solution and the phosphoric acid solution required for the test, and then the diluted, filtered water glass solution and the phosphoric acid solution is poured into the beaker according to the volume ratio of 1:1, and constantly stirred with a glass rod to make it fully react, using the inverted cup method to determine its gel time, the PH of the mixed slurry was measured to record the test data, to avoid test errors for each group tests were performed three times. The average value of gel time was taken after each test was undertaken three times.

2.3 Moraine solidified specimen preparation

In situ moraines have a wide range of particle gradation distribution, with fine to micron-level clay particles as coarse as tens of meters of boulders. Due to the consideration of size effect (Zhu et al., 2020; Zheng et al., 2023) in this experiment, the moraine retrieved from the field was milled, dried, and screened through a 10 mm screen for backup. Tests were undertaken before the drying moraine should be rehydrated to restore the field moisture content after 24 h maintenance. The prepared phosphoric acid-water glass slurry was poured into the mixing bucket and mixed with moraine material, and the slurry was poured into a standard mold measuring 70.7×70.7×70.7 mm. After resting for 24 h for demolding, the specimens were placed in a constant temperature and humidity curing box with a temperature of 20°C and humidity of 90% for 3 days, 7 days and 14 days, respectively. The uniaxial compression test was carried out on the specimens that reached the curing age. This test uses microcomputer-controlled EM3.305 servo single-axis compression equipment, the maximum axial force is 300kN, the displacement control is used to load at a rate of 2 mm/min, and the average value is taken after three parallel tests for each group. The test flow is shown in Figure 4.

2.4 Energy dissipation principle and analysis method

The essence of moraine solidification body deformation damage is the combined result of various dissipation and energy releases. Energy dissipation was used to induce internal damage to produce microcracks, leading to the deterioration of material properties and loss of strength. Energy release triggers sudden damage to the solidified body of the moraine (Huang et al., 2021; Li et al., 2021). Assuming that there is no heat energy dissipation during the deformation and damage of the specimen under load, it is known from the principle of energy conservation:

$$U = U^d + U^e = \int F_N d(l_N) \tag{1}$$

$$U^e = \frac{\sigma_i^2}{2E} = \frac{1}{2E_u}\left[\sigma_1^2 + \sigma_2^2 + \sigma_3^2 - 2\,\bar{\mu}\,(\sigma_1\sigma_2 + \sigma_2\sigma_3 + \sigma_1\sigma_3)\right] \tag{2}$$

$$U^d = U - U^e \tag{3}$$

In the formula: U is the total work done by the external force on the specimen, J; U^d is the energy dissipated inside the specimen due

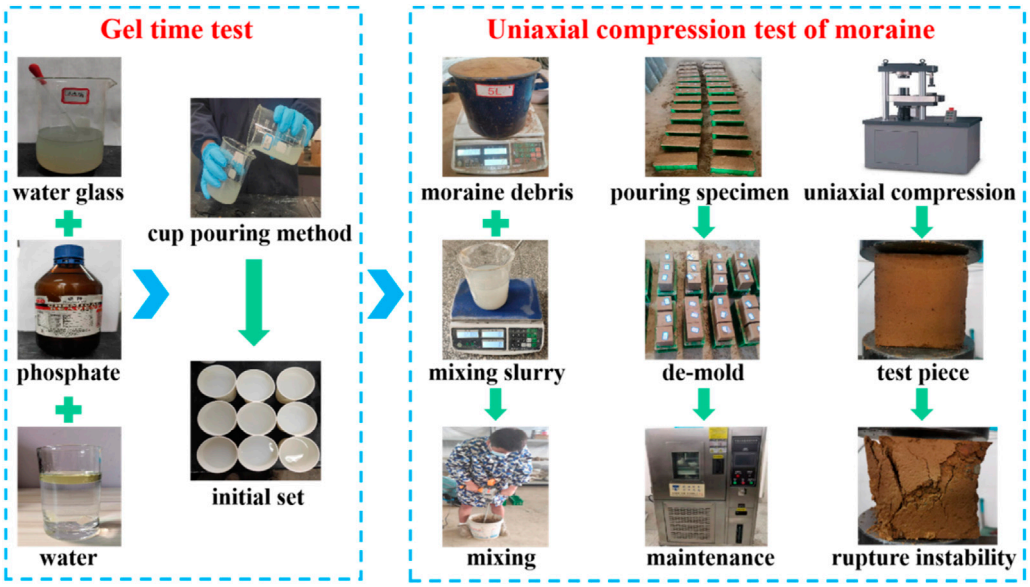

FIGURE 4
Flow chart of moraine solidified specimen preparation.

to the compaction of pores or microcracks and the connection and expansion of microcracks to form a macroscopic rupture surface, J; U^e is the elastic energy accumulated inside the specimen, J; F_N is the axial load, N; l_N is the displacement of the test piece machine indenter in the vertical direction, m; V is the volume of the specimen, m^3; σ and ε are the stress and strain of the specimen respectively; E and μ are the modulus of elasticity and Poisson's ratio of the specimens, respectively.

Dissipative energy density and elastic energy density are introduced to analyze the energy consumption characteristics of the specimen, which are calculated as shown in (4) to (5):

$$\rho_d = \frac{U_d}{V} \tag{4}$$

$$\rho_e = \int_0^{\varepsilon_1} \sigma d\varepsilon \tag{5}$$

The irreversible energy consumed by the pores and microcracks inside the specimen during the bearing process is compacted, or the microcracks expand and connect to form a new fracture surface, which leads to the dissipation of energy. That is, the fracture energy consumed during the deformation and damage of the specimen can be characterized as shown in Equation 6. The relation (7) holds in the linear elastic fracture mechanics when the crack is the stable quasi-static extension, i.e., when the dynamic effect is zero (Dong et al., 2018). At this point, the fracture toughness was introduced to characterize the ability of the specimen to prevent crack expansion, i.e., to reflect the ability of the material to resist brittle fracture (Guo et al., 2005). The expansion law of fracture toughness of moraine solidified specimens is shown in Equation 9:

$$U^d = G_F \tag{6}$$

$$G_F = G_{IC} \tag{7}$$

$$K_{IC}^2 = G_{IC} \times E \tag{8}$$

$$K_{IC} = \sqrt{G_{IC} \times E} = \sqrt{U^d \times E} \tag{9}$$

In the formula: U^d is dissipate energy, J; G_F is the fracture energy, J; G_{IC} is the energy release rate; K_{IC} is the fracture toughness, kPa $\cdot m^{0.5}$; E is the modulus of elasticity.

According to the mechanics of materials and current research (Kivi et al., 2018; Lin et al., 2022; Jiao et al., 2023a; Zou et al., 2023), the area enclosed by the force-displacement curve and the horizontal axis represents the total work done on the material. The area enclosed by the stress-strain curve and the horizontal axis indicates the ability of the material to absorb energy, also known as the strain energy density. The force-displacement curve and stress-strain curve of moraine-cured specimens with a curing age of 14 days and a Baume degree of 20°B e' are used to illustrate the total energy consumption and elastic energy density characterization method. As shown in Figures 5A is the peak load point, the area S_1 is enclosed by its pre-peak deformation phase OA, the x-axis is the total pre-peak energy consumption, and the area S_2 is enclosed by the post-peak deformation phase AB, and the x-axis is the total post-peak energy consumption. As shown in Figure 5B, Point A is the peak stress point, and the area S_1 enclosed by OA and x-axis in its pre-peak deformation phase is the pre-peak elastic energy density, and the area S_2 enclosed by AB and x-axis in the post-peak deformation phase is the post-peak elastic energy density. Since the curves of all post-peak deformation stages cannot be recorded during the actual test, to ensure the comparability of the test data, only the pre-peak change stages of the force-displacement curve and the stress-strain curve are studied in this paper.

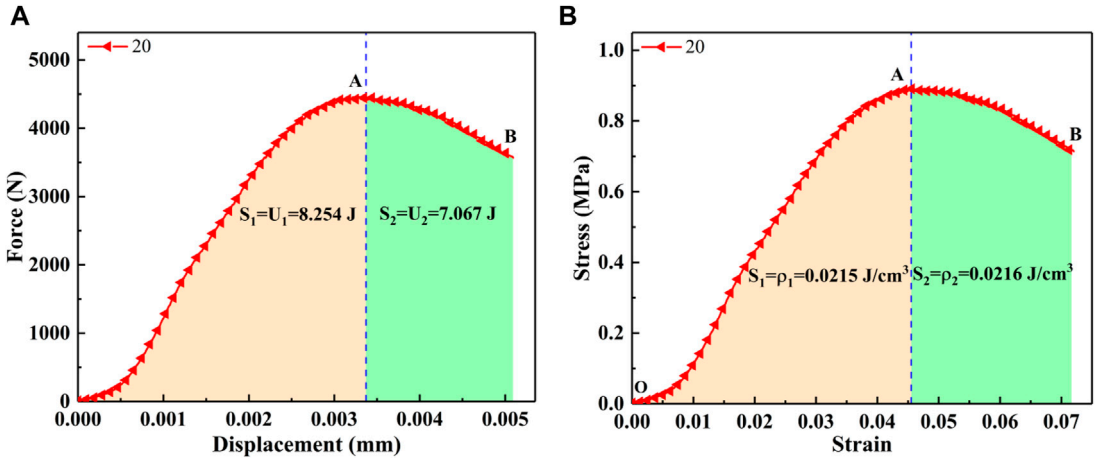

FIGURE 5
Schematic diagram of energy consumption and energy density characterization: **(A)** Schematic representation of energy consumption; **(B)** Schematic representation of elastic energy density.

3 Results and analysis

3.1 Phosphoric acid-water glass slurry gelation test

3.1.1 Mechanism of acidic water-glass gel

Acidic water glass can gel in a neutral or acidic environment, and the gel is not alkaline, so there is no toxicity because there is no alkali leaching, meaning it does not cause pollution to the environment. It is durable and cheaper than alkaline water glass, so it is widely used. The main anions in the water-glass solution are $H_2SiO_4^{2-}$and $H_3SiO_4^-$, and the phosphoric acid solution contains cations H^+. The phosphoric acid solution will be added to the water glass solution in the anion and cation reaction. The chemical reaction equation is as follows:

$$H_2SiO_4^{2-} + H^+ = H_3SiO_{4^-} \quad (10)$$

$$H_3SiO_{4^-} + H^+ = H_4SiO_4 \quad (11)$$

$$H_4SiO_4 + H^+ = H_5SiO_{4^+} \quad (12)$$

In an acidic water-glass solution, the coordination number of the silicic acid molecule is 6. The silicic acid molecule and positive monovalent silicic acid ion carry out a hydroxyl association reaction to form bisilicicic acid, and the specific chemical reaction equation is as follows:

$$H_4SiO_4 + H_5SiO_{4^+} + 2H_2O = H_{13}Si_2O_{10^+} \quad (13)$$

Bisilicicic acid will polymerize again to trisilicicic acid by hydroxyl linkage reaction, and then continue to polymerize to form polysilicicic acid until the formation of silica sol. As the reaction time continues, the SiO_2 particles in the silica sol continue to increase. When the content of SiO_2 particles in the sol exceeds a certain value, these particles condense with each other to form an open and continuous gel network structure. The particles in the gel can intermittently condense to form Si-O-Si bonds, eventually forming a silicon gel with a certain degree of stiffness (Koohestani et al., 2021).

3.1.2 Gel time of phosphate-water glass slurry

As shown in Table 3, the gelation time of phosphoric acid-water glass slurry is non-linearly related to the phosphoric acid addition, and there are mutation points. For example, when the water glass Baume degree is 22°B e', phosphoric acid addition from 10% to 14%, its gel time increased from 2min to 9min relative to each 1% phosphoric acid addition, and its average gel time increased by 1.75min. The gel time increased from 9min to 54min when the acid addition was increased from 14% to 14.5%, and the average gel time increased by 900min for every 1% phosphoric acid addition. The sensitivity of its water glass to the phosphoric acid gel reaction system increases sharply when the phosphoric acid addition exceeds a certain range. As shown in Figure 6, the gel time mutation points of the phosphoric acid-water glass slurry systems with different wavelengths are different. When the phosphoric acid addition amount is less than the phosphoric acid addition amount required for the gel time mutation point, its gel time increases linearly with the increase of the phosphoric acid addition amount. For example, when the water glass Baume degree is 24°B e' its gel time mutation point required phosphoric acid addition is 16.8%. When the phosphoric acid addition is from 10% to 14%, its gel time with phosphoric acid addition follows a linear function y=0.56x-5.07 increasing. This is because the cationic H^+ content in phosphoric acid at this stage is not enough to combine with all the anions $H_2SiO_4^{2-}$ and $H_3SiO_4^-$ ions in the water glass solution, and the H^+ in phosphoric acid at this stage is quickly consumed to form a chain hydroxyl linkage reaction, so the gel time is very short. As phosphoric acid increases, the H^+ ions required to reach the gel time mutation point are sufficient, and the ability of the anions $H_2SiO_4^{2-}$ and $H_3SiO_4^-$ ions in the water glass solution to consume H^+ is limited, resulting in a small pH of the solution, so the gel time increases sharply.

3.2 Moraine slurry curing test

3.2.1 Uniaxial compressive stress-strain curve of moraine curing body

To investigate the effect of phosphoric acid-water glass slurry with different wavelengths on the curing effect of moraines,

TABLE 3 Initial setting time of phosphoric acid-water glass slurry at different wavelengths.

Baume degree of water glass/°Be′	20	22	24	26	28	30
Phosphoric acid concentration/%	Initial setting time/min					
10	6	2	0.8	0.4	0.22	0.08
11	8	3	0.83	0.67	0.3	0.12
12	10	4	1.45	0.72	0.53	0.26
13	24	8	2	1.05	0.58	0.28
13.5	52					
14	>120	9	3	1.56	0.78	0.32
14.5	>120	54				
15	>120	>120	5	2	0.87	0.41
16.8			45			
18.5				35		
20.5					32	
23						37

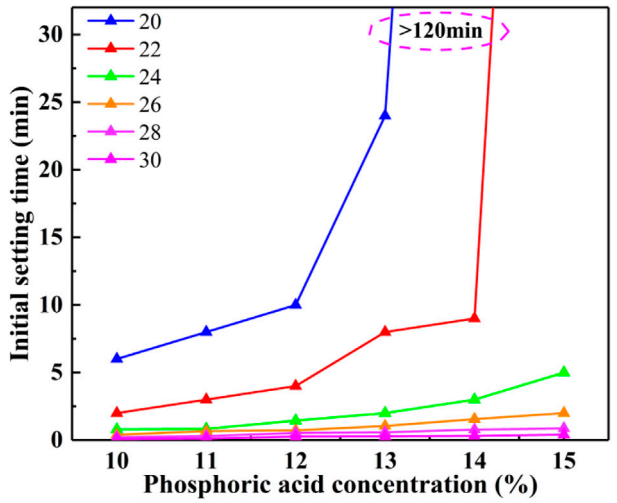

FIGURE 6
Relationship between phosphoric acid concentration and slurry initial setting time at different wavelengths.

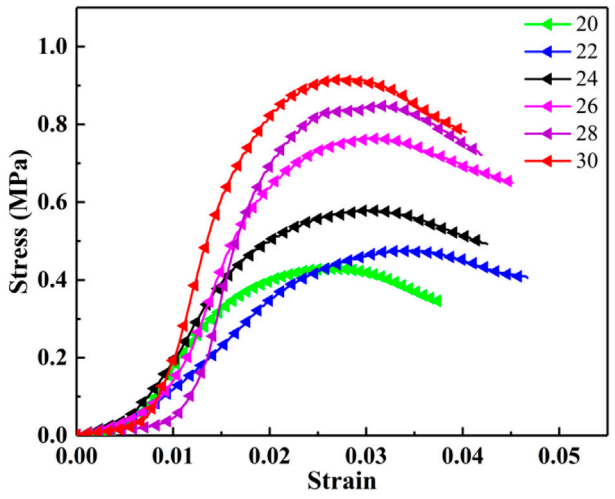

FIGURE 7
Stress-strain curves of solidified bodies of moraines with different baume degrees.

stress-strain curves with a maintenance age of 3 days were selected for analysis. As shown in Figure 7, the stress-strain curves of moraine curing bodies with different wavelengths have the same variation pattern. The stresses all increase slowly with the increase of axial strain and then increase approximately linearly to reach the peak stress point and decay rapidly after reaching the peak stress point. It is suggested that the load-bearing deformation damage of moraine curing bodies with different wavelengths under uniaxial loading are the same type of damage process. In addition, it can be seen from the changing pattern of the curve that the deformation and damage of the solidified body of moraine can all be divided into four stages: initial pressure density, linear elastic deformation, elastic-plastic deformation, and post-peak rupture destabilization. As shown in Figure 8, OA is the initial pressure-density stage. The stress-strain curve of the moraine curing body at the early loading stage is concave, mainly because the moraine curing body is a multi-phase composite damage material. The internal inevitably contains many micro-pores, micro-cracks and bubbles, and other structures. In the uniaxial compression of the moraine curing body, internal micro-pores, micro-cracks, and other structures experience gradual pressure-density closure. The pore volume inside the moraine curing body at this stage gradually decreases with the increase of stress, and the stress growth and radial expansion are smaller. AB is the linear elastic deformation stage. This stage of stress with the increase in strain is a linear growth

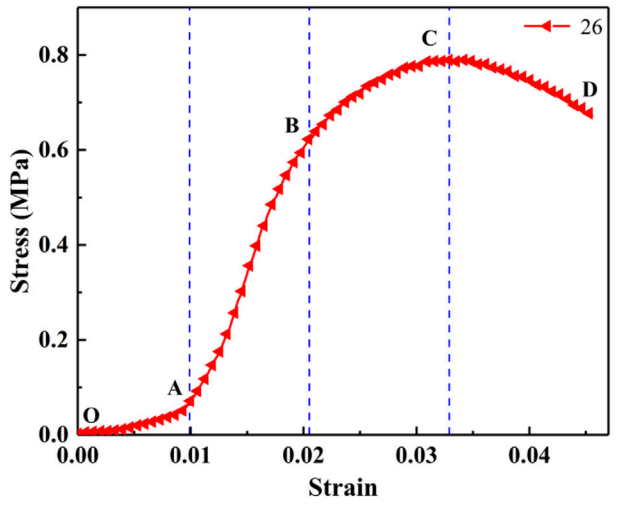

FIGURE 8
Stress-strain curve of moraine solidified specimen.

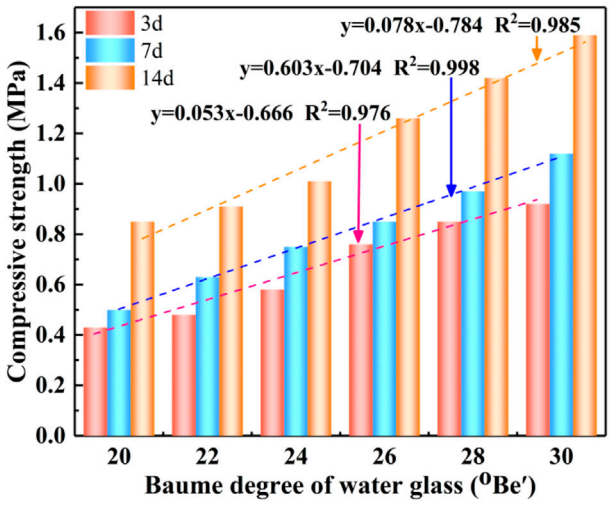

FIGURE 9
Relationship between compressive strength of moraine curing body and Baume degree.

law. It is mainly because a large number of microcracks and microporous structures previously existing inside the moraine curing body have closed, and the damage deformation of the moraine curing body has entered the elastic deformation stage. Its internal microcracks are in a stable development stage, and the damage is also growing, but it has not yet reached the inflection point of the crack damage stress. BC is the elastoplastic deformation stage. This stage curve shows that with the increase of strain, the stress has a small convexity, reaching the bearing limit C point of the specimen. At this time, the moraine solidification internal body undergoes new crack sprouting, crack interlocking, and crack expansion simultaneously. The internal crack grows rapidly during the non-stationary development stage and the evolution of the damage follows a non-stationary growth trend. The internal specimen has not yet generated a macroscopic crack. At the CD for the peak after rupture destabilization stage, the interconnection between the microcracks will form the moraine curing body in the macroscopic formation of a dominant crack after reaching the peak stress. Its direction is nearly parallel to the main stress direction. Damage takes place during the development of the dominant crack and its rupture (Jiao et al., 2023b). At this stage of the moraine curing body, the bearing capacity decreases sharply whilst retaining a certain strength, meaning the curve shows a gradual decrease in stress with the increase in strain law, and damage deformation shows accelerated evolution until the specimen damaged.

3.2.2 Relationship between the influence of water glass baume degree on compressive strength

Figure 9 shows the relationship between the compressive strength of the cured body of moraine under early curing age and different water-glass boehmites. The relevant data were fitted, and the results of the fitting showed that the compressive strength of the moraine curing body under the same curing age condition increased linearly with the increase of the water glass Baume degree, which followed the growth law of the unitary linear regression equation $y = kx - b$. As an example, in the moraine curing body with a curing age of 7 days, with the increase of water glass Baume degree, the compressive strength of the specimens were 0.5, 0.63, 0.75, 0.85, 0.97, and 1.12 MPa, which increased by 26%, 50%, 70%, 94%, and 124%, respectively. This is because the content of SiO_4^{2-} ions in its water-glass solution increases as the Baume degree increases. After mixing phosphoric acid with a water glass solution, PO_4^{3-} ions have a complementary net effect on SiO_4^{2-} ions (Noritake et al., 2022), forming a P-O-Si structure to reduce the degree of hydrolysis of water glass. With the gradual decomposition of the water glass structure, the number of SiO_4^{2-} and OH^- ions in the liquid phase increases, and the solution undergoes a condensation reaction to produce more $nSiO_2$ gel, which fills the pore structure between the moraine particles and plays a bridging role in making the specimen have a better load-bearing capacity. The compressive strength of the moraine-cured body increases with the age of curing under the same water glass Baume degree condition. As an example, the compressive strengths of the specimens were 0.76, 0.85, and 1.26 MPa, respectively, with the increase of the age of curing for the moraine-cured body with a water glass Baume degree of 26 °Be′. The compressive strength of the specimens increased by a factor of 1.1 when the age of moraine curing was increased from 3 days to 7 days. However, when the age of curing was increased from 7 days to 14 days, the strength of the moraine curing showed a sharp increase, and the compressive strength of the specimens increased by a factor of 1.7. This is because the age of curing is 3 days, and the early hydration reaction is not sufficient, the hydration products are relatively independent of each other without cross-linking phenomenon, resulting in the pores between the particles not being filled, so the mechanical strength of the specimen in the early curing is low. However, with the growth of the age of curing, the hydration reaction continues, and the free Ca^{2+} and SiO_4^{2-} undergo a condensation reaction to generate a large number of C-S-H gels (Feng et al., 2022), and the gels lap each other to form a solid, dense skeletal system, which enhances the mechanical strength of the specimens.

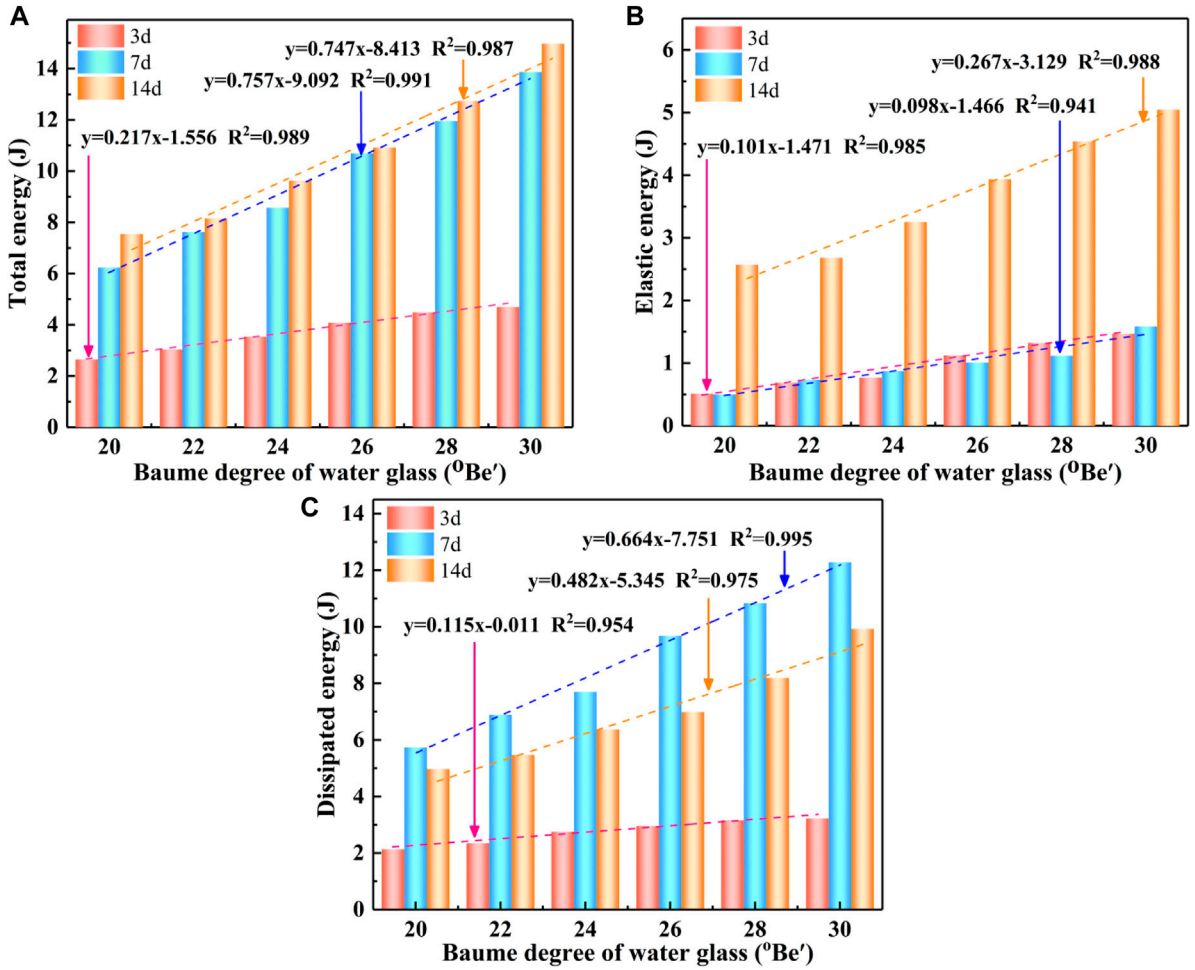

FIGURE 10
Relationship between total energy, elastic energy, dissipative energy, and Baume degree: **(A)** Total energy; **(B)** Elastic energy; **(C)** Dissipation energy.

3.3 Energy consumption characteristics before the peak of moraine solidification body

3.3.1 Relationship between total energy consumption, elastic energy and dissipation energy and water glass baume degree

Through the above energy dissipation principle, the energy of the moraine solidified body in different stages of the uniaxial loading process can be calculated, and the total energy before the peak, elastic energy before the peak, dissipation energy before the peak corresponding to the peak stress point of moraine solidified body under different Baume degree and curing age. The relevant data were fitted, as shown in Figure 9. As can be seen from Figure 10, under the same maintenance age conditions, the total energy before the peak, the elastic energy before the peak, and the dissipation energy before the peak linearly increases with the increase of the water glass Baume degree, which follows the one-dimensional linear regression equation $y = kx - b$ growth law. As shown in Figure 10A, the relationship between the total energy before peak for different curing age conditions is $U_{14d} > U_{7d} > U_{3d}$, but the total energy before peak for curing age 7 days and 14 days is similar and 1.5 times of curing age 3 days, and the total energy before peak increases sharply in phase with the increase of curing age from 3 days to 7 days. When the age of curing was 3 days, the total energy of the specimens with different Baume degree moraine curing bodies was 2.64, 3.04, 3.53, 4.08, 4.48, 4.69 J. As the age of curing increased to 7 days, the total energy before the peak of the specimen was 6.23, 7.63, 8.57, 10.69, 11.95, and 13.87 J. The relative 3 days strength increases were 136%, 151%, 143%, 162%, 167%, and 196%. As shown in Figure 10B, the relationship of peak pre-elastic energy for different curing age conditions is $U^e_{14d} > U^e_{7d} > U^e_{3d}$, and the peak pre-elastic energy of the moraine curing body is similar at the curing ages of 3 days and 7 days, but the elastic energy of the moraine curing body increases sharply as the curing age increases from 7 days to 14 days. As an example, the elastic energy of the specimens with the increase of the curing age was 1.47, 1.59, and 5.05 J. The increase was 8% and 218% respectively. As shown in Figure 10C, the relationship between the peak front dissipation energy for different curing age conditions is $U^d_{7d} > U^d_{14d} > U^d_{3d}$, and the dissipation energy of the specimen with the increase of curing age was 3.22, 12.28, and 9.92 J with increases of 281% and 208%, respectively, for the moraine solidified body with a wavelength of 30 °Be′

The essence of the deformation damage of the solidified body of the moraine is the result of the interaction of the energy of the

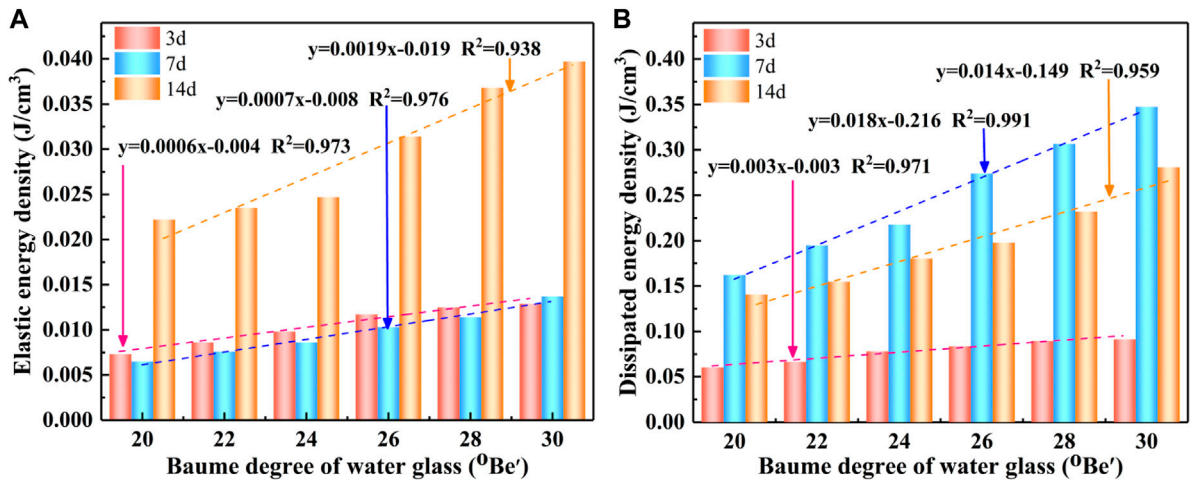

FIGURE 11
Relationship between elastic energy density, dissipative energy density, and Baume degree: **(A)** Elastic energy density; **(B)** Dissipation energy density.

components so that it can be described from the energy point of view: When the curing age is 3 days, the moraine curing body has viscoelastic characteristics, specimen internal hydration reaction is not entirely in the early stage, and at this stage the moraine curing body bearing limit and energy storage capacity are small, resulting in the absorption of smaller energy is sufficient to deformation damage, and at this stage, energy is mainly dissipated in the form of dissipation energy. Although the moraine curing body damage form is mainly manifested in the axial central crack expansion and penetration, the degree of the broken ring depends primarily on the internal microporosity and microfracture structure. Compared to the curing age of 3 days, when the curing age was 7 days, the moraine solidified body specimen's internal hydration reaction into the middle stage generated more C-S-H gel filled parts in the pore structure to improve the energy storage capacity of the specimen. The total energy before the peak of the moraine solidified body increased at this stage, but the number of hydration products inside the specimen was not enough to link the formation of the skeletal structure. This was because the adhesion between the particles was weak, meaning the bearing limit and energy absorption capacity of the moraine solidified body did not grow significantly, increasing the dissipation energy of the specimen. When the curing age was 14 days, the hydration reaction inside the specimen completely entered the final stage, the number of microcracks and microporosity inside the moraine curing body was obviously reduced, the denseness between the particles was better, and the hydration products are cross-linked to each other as the skeleton, meaning the moraine curing body in the later stage of curing has stronger bearing capacity.

3.3.2 Relationship between the effect of water glass baume degree on energy consumption density

Figure 11 shows the relationship between the moraine curing body and energy consumption density for different Baume degrees. As can be seen from Figure 11, the elastic energy density and dissipative energy density of the moraine curing body increase with the increase of water glass Baume degree under the same maintenance age condition, which follows the law of increasing unity linear function $y = kx - b$. Under the same water-glass Baume degree condition, the elastic energy density relationship of the moraine curing body at different curing ages was $\rho_e(14d) > \rho_e(3d) > \rho_e(7d)$, as can be seen from Figure 11A. For example, the elastic energy density of the moraine curing body with the age of curing is 0.0125, 0.0114, 0.0368 J/cm^3 with the increase of the age of maintenance of the moraine curing body with the Baume degree of 28 °Be′. The elastic energy density of the moraine curing body is similar between the curing age of 3 days and 7 days. The elastic energy density of the curing age of 14 days has increased by 2.94 times and 3.23 times relative to 3 days and 7 days, respectively, indicating that the energy absorption capacity of the moraine curing body grows slowly in the early stage of curing and shows a tendency of decreasing first before increasing sharply. From Figure 11B, it can be seen that the dissipative energy density relationship for moraine solidification bodies at different curing ages is $\rho_d(7d) > \rho_d(14d) > \rho_d(3d)$. As an example, the dissipated energy density of the moraine curing body with increasing age of curing is 0.0894, 0.3066, 0.2319 J/cm^3, respectively, with the age of maintenance of the moraine curing body with a Baume degree of 28 °Be′. The dissipation density at the curing age of 7 days was 3.43 and 2.59 times higher than those at 3 days and 14 days, respectively, indicating that the ability to dissipate energy was strongest at the curing age of 7 days.

3.4 Pre-peak fracture characteristics analysis of moraine solidified bodies

Figure 12 shows the peak front fracture toughness *versus* water glass Baume for moraine-cured bodies with different Baume degrees. To qualitatively analyze the variation law of fracture toughness and water glass Baume degree before the peak of the moraine curing body, the relevant data are linearly fitted to show that the pre-peak fracture toughness of the moraine curing body

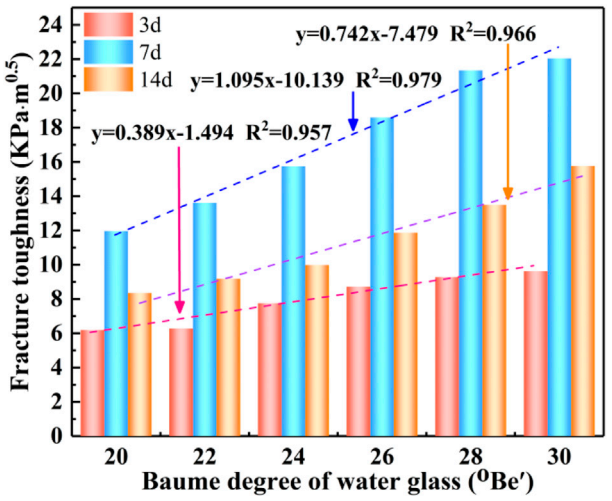

FIGURE 12
Relationship between water glass Baume degree and fracture toughness.

increases linearly with the increase of the water glass Baume degree under the same curing age condition, which follows a linear unity function $y = kx - b$ regular increasing. The pre-peak fracture toughness relationship for moraine cured bodies under the same water glass Baume degree is $K_{IC}(7d) > K_{IC}(14d) > K_{IC}(3d)$. As an example, the fracture toughness of the moraine-cured body specimens with a waviness of 30 °Be′ increased with the age of curing to 9.63, 22.04, and 15.77 kPa · $m^{0.5}$, which increased by 129% and 64%, respectively. This was due to the moraine curing body fracture toughness increasing with the increase of dissipation energy. The moraine curing body specimen is divided into many small units with an increase in dissipation energy. For the internal specimen pores, microcracks are compacted or microcracks expand through each other as energy increases, meaning the moraine curing body internal energy carried by each unit gradually increased, and this part of the energy is irreversible energy (Bi et al., 2020; Bi et al., 2022; Bi et al., 2023). The increased pore structure inside the moraine curing body resulted in the reduction of the force area on each unit and the unit area of the unstressed part increased. As a result, the consumption of irreversible energy gradually increased, meaning the curing body of the moraine was less able to resist fracturing and was at its weakest when the age of curing was 3 days.

4 Discussion

The moraine produced by melting glaciers includes accumulated sediment that is transported into the surrounding landscpae. Surface moraine and side moraine are mostly a mixture of fine particles including soil and stones. When combined with rainfall and ice and snow melt water, moraine soil water content very easily reaches saturation, resulting in the original soil stability structure being destroyed, which quickly collapses to form a debris flow. Moraine debris flow has the characteristics of long movement distance, fast movement speed, and grand scale washout. To effectively prevent and control the debris flow disaster of the moraine in the Pulang copper mine, grouting reinforcement is used to solidify the moraine stratum, solidify the moraine from independent powder fine particles into a whole, and reduce the hazard of debris flow by decreasing the material source of debris flow initiation. It is therefore of great engineering significance to carry out grouting and curing research on moraine soils rich in fine particles to prevent and control moraine debris flow hazards. In this experiment, modified phosphoric acid-water glass slurry was selected as the material used to grout and cure the moraine soil to evaluate the grouting effect by using uniaxial compression equipment. The study analyzed the influence law of water glass Baume degree and the curing age on the energy consumption characteristics and fracture toughness of the grouted fixed body. The calculation formula of the fracture toughness of the moraine was derived and constructed based on the energy consumption principle, the gelling mechanism of phosphoric acid-water glass slurry is revealed, and the suitable slurry ratio is

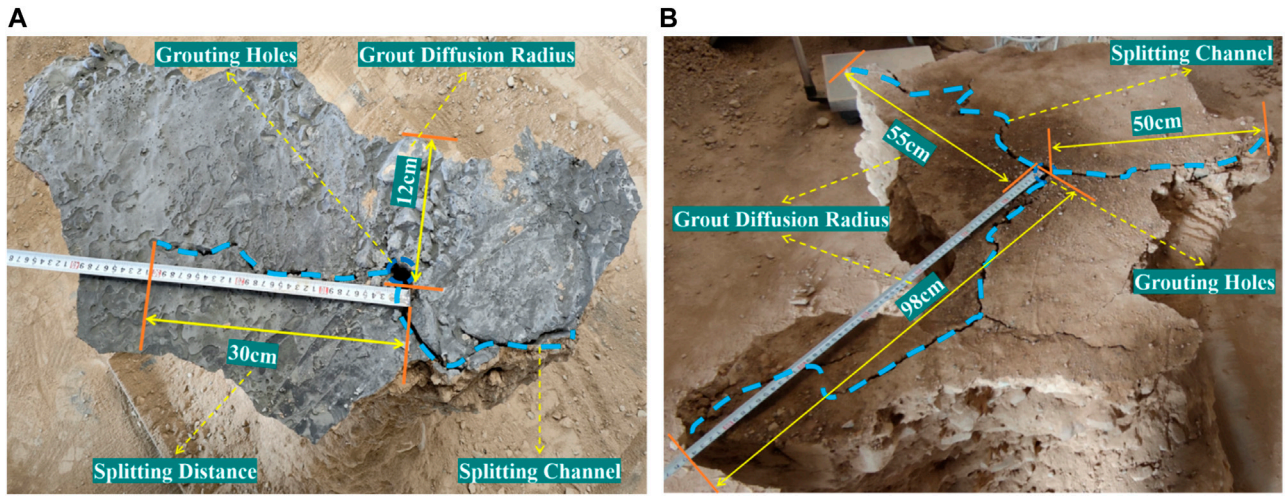

FIGURE 13
Morphology of the cured body of different slurry injections: **(A)** cement slurry; **(B)** phosphoric acid-water glass slurry.

preferred, which is of great significance for the theory of grouting and strengthening of moraine and the mitigation and prevention of glacial debris flow.

Scholars at home and abroad have yet to study the grouting and curing of moraine strata. Yang et al. (Yang et al., 2021) used cement slurry for grouting on moraine slopes with more overhead structures. The effective reinforcement radius was 20–55 cm, and the radius of the hard shell body was only 8–10 cm. In this test, cement slurry and modified phosphoric acid-water glass slurry were used for grouting with a high content of fine particles and poor permeability, and dense moraine formation, respectively, as shown in Figure 13. At the same grouting pressure, the cement slurry spreads in the moraine formation only by splitting, and the effective reinforcement radius is 12–30 cm. While the modified phosphoric acid-water glass grout spreads in the moraine formation by penetration and splitting together, the effective reinforcement radius of the slurry was 50–100cm, and the penetration distance was 20–45 cm. The curing volume was much larger than that of the cement slurry, which indicates that the grouting material has a better grouting effect on the moraine formation with abundant fine particles. This study was mainly based on the principle of energy consumption and evaluates the grouting effect of slurry. Results indicated that the slurry in the moraine stratum diffusion distribution law needs to be further improved, while the test found that the strength of the modified phosphoric acid-water glass slurry, which was used to cure the moraine, was less than 3 MPa. For moraine with a rich content of fine particles, further in-depth study of the poor permeability of the stratum should be undertaken, with the aim of developing a strong injectability and high curing strength of the material.

5 Conclusion

In order to study the curing effect of modified phosphoric acid-water glass slurry on moraine after grouting, the present study investigated initial setting times for phosphoric acid-water glass slurry for grouting and the gelation mechanism of the slurry through the slurry gelation test. The influence law of water glass Baume degree and maintenance age on the mechanical properties, energy consumption characteristics and fracture characteristics of the moraine curing body were analyzed with the help of uniaxial compression test. The research conclusions are as follows.

1) In the phosphoric acid-water glass slurry system, the gel time increases with the addition of phosphoric acid but has a mutation point. The gel time increases linearly with increasing phosphoric acid addition when the required phosphoric acid addition is not reached at the mutation site. After reaching the required phosphoric acid addition at the mutation point, the sensitivity of the water glass to phosphoric acid in the gelation reaction increases sharply, leading to a sharp increase in gelation time. The amount of phosphoric acid addition required for the abrupt gel time change point increases with increasing water glass Baume.
2) The axial stress of the moraine curing body under uniaxial compression is nonlinear with the increase of axial strain. Peak stress increases with increasing water glass Baume degree. The stress-strain curves of different wavelength moraine curing bodies have the same change pattern. Stress is related to the increase of axial strain, which, at first, slowly increases and then shows a near linear increase to reach the peak stress point. The peak stress point is reached after the rapid decay. Its damage evolution process can be divided into four stages the initial pressure density, linear elastic deformation, and elastoplastic deformation after the peak rupture instability.
3) The compressive strength, total pre-peak energy, pre-peak elastic energy, pre-peak dissipation energy, elastic energy density, dissipation energy density, and pre-peak fracture toughness of the moraine curing body under the same curing age conditions show a linear increasing law with the increase of water glass Baume degree. The compressive strength, pre-peak elastic energy, and pre-peak elastic energy density of the moraine curing body increased with the increase of the curing age under different curing age conditions. Despite this, the increase was not the same, and the curing age increased slowly from 3 days to 7 days and increased rapidly from 7 days to 14 days.
4) Moraine solidification body in the curing age of 7 days and 14 days occurs when the total energy before the peak is similar and 1.5 times the total energy before the height of the curing age of 3 days. The curing age from 3days to 7 days and the total energy before the peak increases sharply and in 7 days to 14 days as soon as the growth is slow. The pre-peak dissipation energy, dissipation energy density, and pre-peak fracture toughness of the moraine curing body were at their maximum at a curing age of 7 days and minimum at a curing age of 3 days.

Data availability statement

The original contributions presented in the study are included in the article/supplementary material, further inquiries can be directed to the corresponding author.

Author contributions

Investigation, Z-rL and S-yW; methodology, Z-rL; conceptualization, M-gJ and S-yW; writing—original draft preparation, Z-rL; funding acquisition, S-yW; writing—review and editing, Z-rL and M-gJ; supervision, Q-tZ and WS; visualization, X-lF; validation, CC; data curation, W-lL. All authors contributed to the article and approved the submitted version.

Funding

This research was financially supported by the National Natural Science Foundation of China (Grant No. 51964023), the Yunnan Major Scientific and Technological Projects (Grant No. 202202AG050014), and by Yunnan Fundamental Research Projects (Grant No. 202101BE070001-038; 202201AT070146).

Conflict of interest

Z-rL, X-lF, Q-tZ were employed by Yunnan Diqing Non-Ferrous Metal Co, Ltd.

The remaining authors declare that the research was conducted in the absence of any commercial or financial relationships that could be construed as a potential conflict of interest.

Publisher's note

References

Begam, S., Sen, D., and Dey, S. (2018). Moraine dam breach and glacial lake outburst flood generation by physical and numerical models. *J. Hydrol.* 563, 694–710. doi:10.1016/j.jhydrol.2018.06.038

Bi, J., Liu, P., and Gan, F. (2020). Effects of the cooling treatment on the dynamic behavior of ordinary concrete exposed to high temperatures. *Constr. Build. Mat.* 248, 118688. doi:10.1016/j.conbuildmat.2020.118688

Bi, J., Ning, L., Zhao, Y., Wu, Z., and Wang, C. (2023). Analysis of the microscopic evolution of rock damage based on real-time nuclear magnetic resonance. *Rock Mech. Rock Eng.* 56, 3399–3411. doi:10.1007/s00603-023-03238-x

Bi, J., Tang, J., Wang, C., Quan, D., and Teng, M. (2022). Crack coalescence behavior of rock-like specimens containing two circular embedded flaws. *Lithosphere* 11, 9498148. doi:10.2113/2022/9498148

Coulter, S., and Martin, C. (2006). Effect of jet-grouting on surface settlements above the Aeschertunnel, Switzerland. *Tunn. Undergr. Sp. Tech.* 21, 542–553. doi:10.1016/j.tust.2005.07.005

Cui, Y., Tan, Z., and An, C. (2022). Research and application of multi-functional acrylic resin grouting material. *Constr. Build. MATER* 359, 129381. doi:10.1016/j.conbuildmat.2022.129381

Dong, L., Jin, L., Xui, D., and Liu, J. (2018). A theoretical method to predict the mechanical properties of concrete considering of the size effect in material. *J. Hydraul. Eng.* 49, 464–473. doi:10.13243/j.cnki.slxb.20171162

Evans, D., Smith, I., Gosse, J., and Galloway, J. (2021). Glacial landforms and sediments (landsystem) of the smoking hills area, northwest territories, Canada: implications for regional pliocene – pleistocene laurentide ice sheet dynamics. *Quat. Sci. Rev.* 262, 106958. doi:10.1016/j.quascirev.2021.106958

Fan, H., Xu, Q., Lai, J., Liu, T., Zhu, Z., Zhu, Y., et al. (2023). Stability of the loess tunnel foundation reinforced by jet grouting piles and the influence of reinforcement parameters. *Transp. Geotech.* 40, 100965. doi:10.1016/j.trgeo.2023.100965

Feng, H., Liang, J., Pang, Y., Zhao, X., Wang, Y., and Sheikh, S. (2022). Effects of the fly ash and water glass on the mechanical properties and water stability of the high ductile magnesium phosphate cement-based composite. *Constr. Build. MATER* 333, 127395. doi:10.1016/j.conbuildmat.2022.127395

Gao, T., Sun, W., Liu, Z., and Cheng, H. (2022). Investigation on fracture characteristics and failure pattern of inclined layered cemented tailings backfill. *Constr. Build. Mater* 343, 128110. doi:10.1016/j.conbuildmat.2022.128110

Guo, X., Fang, K., and Leng, F. (2005). Analysis of the theory of fracture energy of concrete. *J. Harbin Inst. Technol.* 37, 1219–1222. doi:10.3321/j.issn:0367-6234.2005.09.017

Hart, J. (1998). The deforming bed/debris-rich basal ice continuum and its implications for the formation of glacial landforms (flutes) and sediments (melt-out till). *Quat. Sci. Rev.* 17, 737–754. doi:10.1016/S0277-3791(98)00065-6

Huang, Z., Yilmaz, E., and Cao, S. (2021). Analysis of strength and microstructural characteristics of mine backfills containing fly ash and desulfurized gypsum. *Minerals* 11, 409. doi:10.3390/min11040409

Jiao, H., Yang, W., Ruan, Z., Yu, J., Liu, J., and Yang, Y. (2023a). The micro-scale mechanism of tailings thickening processing from metal mines. *Int. J. Min. Metall. Mater* 2023, 2587. doi:10.1007/s12613-022-2587-0

Jiao, H., Zhang, W., Yang, Y., Chen, X., Yang, L., Shen, H., et al. (2023b). Static mechanical characteristics and meso-damage evolution characteristics of layered backfill under the condition of inclined interface. *Constr. Build. Mater* 366, 130113. doi:10.1016/j.conbuildmat.2022.130113

Kivi, I., Ameri, M., and Molladavoodi, H. (2018). Shale brittleness evaluation based on energy balance analysis of stress-strain curves. *J. Pet. Sci. Eng.* 167, 1–19. doi:10.1016/j.petrol.2018.03.061

Koohestani, B., Mokhtari, P., Yilmaz, E., Mahdipour, F., and Darban, A. (2021). Geopolymerization mechanism of binder-free mine tailings by sodium silicate. *Constr. Build. Mater* 268, 121217. doi:10.1016/j.conbuildmat.2020.121217

Kumar, S., Tiwari, G., Parameswaran, V., and Das, A. (2022). Rate-dependent mechanical behavior of jointed rock with an impersistent joint under different infill conditions. *J. Rock Mech. Geotech. Eng.* 14, 1380–1393. doi:10.1016/j.jrmge.2022.05.002

Li, C., Wang, R., Gu, D., Wang, J., Chen, X., Zhou, J., et al. (2022). Temperature and ice form effects on mechanical behaviors of ice-richmoraine soil of Tianmo valley nearby the Sichuan-Tibet Railway. *Eng. Geol.* 305, 106713. doi:10.1016/j.enggeo.2022.106713

Li, J., Yilmaz, E., and Cao, S. (2021). Influence of industrial solid waste as filling material on mechanical and microstructural characteristics of cementitious backfills. *Constr. Build. Mater* 299, 124288. doi:10.1016/j.conbuildmat.2021.124288

Li, L., Tu, W., Shi, S., Chen, J., and Zhang, Y. (2016). Mechanism of water inrush in tunnel construction in karst area. *Geomat. Nat. HAZ RISK* 7, 35–46. doi:10.1080/19475705.2016.1181342

Lin, H., Liu, J., Yang, J., Ran, L., Ding, G., Wu, Z., et al. (2022). Analysis of damage characteristics and energy evolution of salt rock under triaxial cyclic loading and unloading. *J. Energy Storage* 56, 106145. doi:10.1016/j.est.2022.106145

Liu, X., Chen, H., Liu, Q., Liu, B., and He, J. (2022). Modelling slurry flowing and analyzing grouting efficiency under hydro-mechanical coupling using numerical manifold method. *Eng. Anal. BOUND Elem.* 134, 66–78. doi:10.1016/j.enganabound.2021.09.030

Luo, F., Liu, E., and Zhu, Z. (2019). A strength criterion for frozen moraine soils. *COLD Reg. Sci. Technol.* 164, 102786. doi:10.1016/j.coldregions.2019.102786

Marr, J. G., Anders, E., Harbitz, C., Imran, J., and Harff, P. (2002). Numerical simulation of mud-rich subaqueous debris flows on the glacially active margins of the Svalbard–Barents Sea. *Mar. Geol.* 188, 351–364. doi:10.1016/S0025-3227(02)00310-9

Medeu, A., Popov, N., Blagovechshenskiy, V., Askarova, M., Medeu, A., Ranova, S., et al. (2022). Moraine-dammed glacial lakes and threat of glacial debris flows in South-East Kazakhstan. *Earth-Sci. Rev.* 229, 103999. doi:10.1016/j.earscirev.2022.103999

Meng, Z., Lyu, L., Xu, M., Yu, G., Ma, C., Wang, Z., et al. (2023). Effects of frequent debris flows on barrier lake formation, sedimentation and vegetation disturbance, Palongzangbo River, Tibetan Plateau. *CATENA* 220, 106697. doi:10.1016/j.catena.2022.106697

Noritake, F., Sato, T., Yamamoto, A., Wakabayashi, D., Urakawa, S., and Funamori, N. (2022). Structure of sodium silicate water glass—X-Ray scattering experiments and force-field molecular dynamics simulations. *J. NON-CRYST SOLIDS* 579, 121370. doi:10.1016/j.jnoncrysol.2021.121370

Peng, D., Zhang, L., Jiang, R., Zhang, S., Shen, P., Lu, W., et al. (2022). Initiation mechanisms and dynamics of a debris flow originated from debris-ice mixture slope failure in southeast Tibet, China. *Eng. Geol.* 307, 106783. doi:10.1016/j.enggeo.2022.106783

Salimian, M., Baghbanan, A., Hashemolhosseini, H., Dehghanipoodeh, M., and Norouzi, S. (2017). Effect of grouting on shear behavior of rock joint. *Int. J. ROCK Mech. Min.* 98, 159–166. doi:10.1016/j.ijrmms.2017.07.002

Sui, W., Liu, J., Hu, W., Qi, J., and Zhan, K. (2015). Experimental investigation on sealing efficiency of chemical grouting in rock fracture with flowing water. *Tunn. Undergr. Sp. Tech.* 50, 239–249. doi:10.1016/j.tust.2015.07.012

Weng, L., Wu, Z., Zhang, S., Liu, Q., and Chu, Z. (2022). Real-time characterization of the grouting diffusion process in fractured sandstone based on the low-field nuclear magnetic resonance technique. *Int. J. ROCK Mech. Min.* 152, 105060. doi:10.1016/j.ijrmms.2022.105060

Yang, D., Wang, J., Shi, S., and Yang, D. (2021). Reinforcement of the moraine slope with steel screen pipe grouting. *Drill. Eng.* 48, 89–95. doi:10.12143/j.ztgc.2021.08.014

Yi, Q., Pu, H., Preuße, A., Bian, Z., and Wu, J. (2022). Effect of dry-wet cycles on dynamic mechanic and microstructure of cemented broken mudstone. *Constr. Build. MATER* 357, 129347. doi:10.1016/j.conbuildmat.2022.129347

Zaginaev, V., Petrakov, D., Erokhin, S., Meleshko, A., Stoffel, M., and Ballesteros-Cánovas, J. (2019). Geomorphic control on regional glacier lake outburst flood and

debris flow activity over northern Tien Shan. *Glob. Planet. Change* 176, 50–59. doi:10.1016/j.gloplacha.2019.03.003

Zhang, C., Yang, J., Fu, J., Wang, S., Yin, J., Xie, Y., et al. (2021). Cement based eco-grouting composite for pre-reinforcement of shallow underground excavation in vegetation protection area. *Tunn. Undergr. Sp. Tech.* 118, 104188. doi:10.1016/j.tust.2021.104188

Zhang, G., Xiao, M., Zhang, Y., Liu, H., Zhuo, L., Xie, H., et al. (2022). Experimental and numerical study on the mechanical properties of compressively precracked sandstone repaired by grouting. *Constr. Build. MATER* 350, 12881. doi:10.1016/j.conbuildmat.2022.128816

Zhao, J., Lu, C., Deng, L., and Liu, G. (2018). Impacts of simulated acid solution on the disintegration and cation release of purple rock (mudstone) in Southwest China. *GEOMORPHOLOGY* 316, 35–43. doi:10.1016/j.geomorph.2018.05.009

Zheng, Y., Zhang, Y., Zhuo, J., Zhang, P., and Hu, S. (2023). Mesoscale synergistic effect mechanism of aggregate grading and specimen size on compressive strength of concrete with large aggregate size. *Constr. Build. MATER* 367, 130346. doi:10.1016/j.conbuildmat.2023.130346

Zhu, H., Alam, S., and Loukili, A. (2020). An experimental investigation on the correlation between the aggregate size effect and the structural size effect. *Eng. Fract. Mech.* 234, 107101. doi:10.1016/j.engfracmech.2020.107101

Zou, C., Li, J., Liu, K., and Zhao, X. (2023). Dynamic cracking process of rock interpreted by localized strain-rate, rate-dependent strength field and transition strain-rate. *Int. J. ROCK Mech. Min.* 163, 105340. doi:10.1016/j.ijrmms.2023.105340